# Time Scales in Dynamical Sauter-Schwinger Pair Creation: Dependence on Transverse Momentum

D.  $SAH^{a,b,*}$  AND M.P.  $SINGH^{a,b}$ 

<sup>a</sup> Theory and Simulations Lab, Theoretical and Computational Physics Section, Raja Ramanna Centre for Advanced Technology, Indore 452013, India

<sup>b</sup>Homi Bhabha National Institute, Training School Complex, Anushakti Nagar, Mumbai 400094, India

Received: 15.07.2025 & Accepted: 25.08.2025

Doi: 10.12693/APhysPolA.148.149

\*e-mail: dsah129@gmail.com

We investigate the dynamics of particle creation in a time-dependent, spatially uniform Sauter pulsed electric field by analyzing the evolution of the one-particle momentum distribution function. This quantity provides key insights into the non-perturbative process of electron-positron pair production in strong-field quantum electrodynamics. The longitudinal momentum spectrum of the created particles exhibits rich features, including spectral splitting and oscillatory behavior, particularly around the time when the electric field approaches zero. These oscillations can be attributed to quantum interference effects during the dynamical evolution. By examining the temporal evolution of the spectrum, we identify three distinct characteristic time scales associated with key spectral transitions, which depend on the transverse momentum  $p_{\perp}$ . We find out approximate expressions for the relevant time scales as functions of  $p_{\perp}$ , the pulse duration  $\tau$ , and the field strength  $E_0$ , offering a clearer understanding of the interplay between field parameters and the dynamics of pair production.

topics: particle production, non-perturbative field theory, dynamical scaling, strong-field quantum electrodynamics

# 1. Introduction

The discovery of the positron following Dirac's formulation of the relativistic wave equation [1] marked a foundational milestone in the development of quantum field theory. Shortly after its theoretical prediction, the positron was experimentally confirmed [2], firmly establishing the existence of antimatter. It was soon recognized that quantum fluctuations of the electron-positron field lead to nonlinear quantum electrodynamic (QED) phenomena, such as light-by-light scattering in the presence of classical electromagnetic backgrounds [3]. Among the most striking consequences of this quantum vacuum structure is the prediction that a sufficiently strong electric field can induce the spontaneous creation of real electron-positron pairs from the vacuum [4]. This concept was later formalized within QED through a non-perturbative analysis of the one-loop effective action [5, 6], whose imaginary part encodes the pair production probability and signals the vacuum instability. For a static, spatially homogeneous electric field, Schwinger derived the pair production rate as

$$\Gamma = \frac{(eE)^2}{4\pi^3} \exp\left(-\frac{\pi m^2}{|eE|}\right),\tag{1}$$

where m and e are the electron mass and charge, respectively. This result reveals the non-perturbative nature of the process, with an exponential suppression unless the field strength approaches the socalled critical value  $E_c = m^2/|e| \approx 1.32 \times 10^{18} \text{ V/m}.$ Although such extreme fields remain inaccessible in current laboratory experiments, they are believed to occur in certain astrophysical environments, such as the vicinity of magnetars or during early cosmological epochs [7]. Despite the challenge of directly probing this regime, experimental progress has been made in studying strong-field QED effects. For instance, multiphoton pair production was observed at Stanford Linear Accelerator Center (SLAC) [8], and future laser facilities such as Extreme Light Infrastructure (ELI) and X-ray Free Electron Laser (XFEL) [9, 10] are designed to approach the field strengths required for observing Schwinger-type pair creation. These advances have sparked extensive theoretical interest in vacuum pair production under more realistic field profiles, particularly time-dependent electric fields generated by ultrashort laser pulses. Pair creation mechanisms are typically divided into two broad regimes [11, 12], i.e., non-perturbative tunneling, dominant in slowly varying fields ( $\gamma \ll 1$ ), and multiphoton absorption, relevant in rapidly oscillating fields ( $\gamma \gg 1$ ). The Keldysh parameter  $\gamma = \frac{m\omega}{|eE_0|}$ ,

where  $\omega$  is the field frequency and  $E_0$  its amplitude, governs the transition between these two domains. While Schwinger's original result applies to an idealized, constant background, realistic experimental conditions involve ultrashort, pulsed, and spatially localized electric fields [13–16]. When the pulse duration becomes comparable to the electron Compton time  $t_c=1/m\approx 1.3\times 10^{-21}$  s, the static-field approximation breaks down. In such scenarios, pair production must be understood as a genuinely time-dependent, non-equilibrium quantum process.

To describe this, real-time quantum kinetic approaches have been developed. One widely used framework is the quantum Vlasov equation [16–19], which enables calculation of the time evolution of the single-particle distribution function  $f(\mathbf{p}, t)$ . These approaches naturally incorporate initial vacuum conditions, non-Markovian dynamics, and memory effects [20]. Moreover, they support a quasiparticle interpretation of vacuum excitations, wherein each mode of the distribution evolves through a characteristic three-stage pattern [20–23], i.e., (i) a quasiparticle electron-positron plasma (QEPP) forming under the action of the external field, (ii) a transient regime characterized by strong oscillatory behavior, and (iii) a residual electronpositron plasma (REPP) in which the momentum distribution stabilizes.

Notably, this dynamical structure resembles the early-time evolution of the quark-gluon plasma (QGP) created in ultra-relativistic heavy-ion collisions. In quantum chromodynamics (QCD), strong longitudinal color-electric fields — analogous to external fields in QED — can lead to quark—antiquark pair production via a non-Abelian generalization of the Schwinger mechanism. The initial QCD excitations mirror the QEPP phase, while the intermediate glasma stage [24–26] displays collective field oscillations and plasma instabilities analogous to the QED transient regime. Ultimately, QGP relaxes toward a quasi-equilibrium state, comparable to the REPP. This analogy underscores the wider applicability of kinetic theory methods and the quasiparticle picture in the study of out-of-equilibrium quantum fields.

While much of the literature has focused on the longitudinal momentum dynamics, i.e., the evolution of modes aligned with the direction of the electric field, the role of transverse momentum has been relatively less explored. This is despite its importance for computing physically relevant observables such as total pair number density, electric current, and entropy [23, 27–31]. Previous studies have investigated the time evolution of individual longitudinal momentum modes [16, 25, 32] and the complete longitudinal momentum spectrum [18, 33, 34]. However, the time-dependent behavior of transverse momentum modes and their effect on the underlying dynamics of pair formation have received comparatively little attention.

A recent study [35] explored the real-time evolution of the longitudinal momentum spectrum in a pulsed Sauter-type electric field and identified nontrivial dynamical substructures, leading to insights into characteristic time scales associated with particle formation [31, 36]. However, this analysis neglected the transverse degrees of freedom. To date, no systematic framework exists that classifies the evolution of the spectrum while incorporating transverse momentum dependence, or explains how this dependence affects the timing and features of the various dynamical stages. In this work, we aim to address this gap. We investigate the dynamics of electron-positron pair production in a time-dependent, spatially uniform Sauter-type pulsed electric field of the form  $E(t) = E_0 \operatorname{sech}^2\left(\frac{t}{\tau}\right)$ , where  $E_0$  is the peak field strength and  $\tau$  is the pulse duration. This widely studied configuration serves as a benchmark for understanding temporal effects in pair creation [16, 20, 21].

We compute the time evolution of the singleparticle distribution function  $f(\mathbf{p},t)$  in the quasiparticle framework. Focusing first on zero transverse momentum, we analyze the dynamics of the longitudinal spectrum and observe a transition from an initial unimodal peak to a bimodal intermediate structure with pronounced oscillations, which eventually settles into a smooth, single-peaked profile at later times. These features enable us to identify three characteristic time scales associated with quasiparticle formation, coherence oscillations, and final stabilization. We then explore how these time scales depend on transverse momentum. Our results reveal a nontrivial dependence, which we systematically classify. This leads to a deeper understanding of the role of transverse degrees of freedom in the real-time dynamics of vacuum pair production, filling an important gap in the literature and providing new insight into the momentum-space structure of quantum vacuum instability.

This paper is organized as follows. In Sect. 2, we introduce the theoretical formalism based on [37, 38]. In Sect. 3, we analyze the results. In the last section, we provide a brief conclusion.

Throughout the paper, we use natural units and set  $\hbar = c = m = |e| = 1$ , and express all variables in terms of the electron mass unit.

#### 2. Theory

# 2.1. Equations of motion and canonical quantization

A sufficiently strong electric field can destabilize the vacuum, leading to the non-perturbative production of charged particle—antiparticle pairs. To describe this phenomenon in the context of QED, we begin with the Dirac equation in the presence of a classical electromagnetic background field

$$(i\gamma^{\mu}\partial_{\mu} - e\gamma^{\mu}A_{\mu} - m) \Psi(\mathbf{x}, t) = 0, \tag{2}$$

where  $A^{\mu}$  is the external gauge potential. We consider a spatially homogeneous, time-dependent electric field, represented in the Hamiltonian gauge by the four-potential

$$A_{\mu} = (0, 0, A(t)).$$
 (3)

This configuration yields a purely electric field given by

$$E(t) = -\frac{\mathrm{d}A(t)}{\mathrm{d}t},\tag{4}$$

with no magnetic field component,

$$\boldsymbol{B} = \nabla \times \boldsymbol{A} = 0,\tag{5}$$

ensuring the field is homogeneous in space and varies only with time.

Such field configurations can be realized experimentally, for instance, by two counter-propagating laser pulses forming a standing wave. In QED, pair production is allowed only if at least one of the two Lorentz invariants,

$$\frac{1}{4}F_{\mu\nu}F^{\mu\nu} = \frac{1}{2}(\mathbf{E}^2 - \mathbf{B}^2),\tag{6}$$

$$\frac{1}{4}F_{\mu\nu}\tilde{F}^{\mu\nu} = \boldsymbol{E} \cdot \boldsymbol{B},\tag{7}$$

is nonzero [39, 40]. In our case, only the invariant in (6) contributes, allowing for nontrivial pair production.

The first step is the introduction of an ansatz

$$\Psi(\boldsymbol{x},t) =$$

$$\left[i\gamma^{0}\partial_{t} + \gamma^{k}p_{k} - e\gamma^{3}A(t) + m\right] e^{i\boldsymbol{p}\cdot\boldsymbol{x}} \psi_{\boldsymbol{p}}^{(\pm)}(t) R_{r},$$
(8)

where k = 1, 2, 3 and  $(\pm)$  label the positive and negative frequency components. The spinors  $R_1$  and  $R_2$  are eigenvectors of  $\gamma^0 \gamma^3$ , thus

$$R_{1} = \begin{pmatrix} 0 \\ 1 \\ 0 \\ -1 \end{pmatrix}, \quad R_{2} = \begin{pmatrix} 1 \\ 0 \\ -1 \\ 0 \end{pmatrix}, \tag{9}$$

normalized such that  $R_r^{\dagger}R_s = 2\delta_{rs}$ .

Substituting (8) into the Dirac equation leads to a second-order differential equation for the timedependent mode functions

$$\left(\partial_t^2 + i e E(t) + \omega^2(\boldsymbol{p}, t)\right) \psi_{\boldsymbol{p}}(t) = 0, \tag{10}$$

where

$$\omega^{2}(\mathbf{p},t) = p_{\perp}^{2} + (p_{\parallel} - eA(t))^{2} + m^{2}.$$
 (11)

Here,  $p_{\parallel}=p_3$  is the momentum along the field direction, and  $p_{\perp}=\sqrt{p_1^2+p_2^2}$  is the transverse momentum.

In the framework of second quantization, the Dirac field operator is expanded as

$$\hat{\Psi}(\boldsymbol{x},t) = \sum_{r} \int \frac{\mathrm{d}^{3} \boldsymbol{p}}{(2\pi)^{3}} \times \left[ \Psi_{\boldsymbol{p}r}^{(+)}(\boldsymbol{x},t) \, \hat{b}_{\boldsymbol{p}r} + \Psi_{-\boldsymbol{p}r}^{(-)}(\boldsymbol{x},t) \, \hat{d}_{\boldsymbol{p}r}^{\dagger} \right], \tag{12}$$

where  $\hat{b}_{pr}$  and  $\hat{d}_{pr}^{\dagger}$  are the annihilation and creation operators for electrons and positrons, respectively. These obey standard fermionic anti-commutation relations

$$\{\hat{b}_{\boldsymbol{p}r}, \hat{b}_{\boldsymbol{p}'r'}^{\dagger}\} = \{\hat{d}_{\boldsymbol{p}r}, \hat{d}_{\boldsymbol{p}'r'}^{\dagger}\} = \delta(\boldsymbol{p} - \boldsymbol{p}') \,\delta_{rr'}. \tag{13}$$

To extract physical observables, such as the particle spectrum, we perform a Bogoliubov transformation to a quasiparticle basis with time-dependent operators  $\hat{B}_{pr}(t)$  and  $\hat{D}_{pr}(t)$ , i.e.,

$$\hat{B}_{pr}(t) = \alpha_{p}(t)\,\hat{b}_{pr} + \beta_{p}(t)\,\hat{d}_{-pr}^{\dagger},\tag{14}$$

$$\hat{D}_{\boldsymbol{p}r}(t) = \alpha_{-\boldsymbol{p}}(t)\,\hat{d}_{\boldsymbol{p}r} - \beta_{-\boldsymbol{p}}(t)\,\hat{b}_{-\boldsymbol{p}r}^{\dagger},\tag{15}$$

subject to the normalization condition

$$|\alpha_{\mathbf{p}}(t)|^2 + |\beta_{\mathbf{p}}(t)|^2 = 1.$$
 (16)

In this representation, the field operator becomes

$$\hat{\Psi}(\boldsymbol{x},t) = \sum_{r} \int \frac{\mathrm{d}^{3} \boldsymbol{p}}{(2\pi)^{3}}$$

$$\times \left[ \Phi_{\boldsymbol{p}r}^{(+)}(\boldsymbol{x},t) \, \hat{B}_{\boldsymbol{p}r}(t) + \Phi_{-\boldsymbol{p}r}^{(-)}(\boldsymbol{x},t) \, \hat{D}_{\boldsymbol{p}r}^{\dagger}(t) \right], \quad (17)$$

where the spinors  $\Phi_{\boldsymbol{p}r}^{(\pm)}(\boldsymbol{x},t)$  are given by

$$\Phi_{\mathbf{p}r}^{(+)}(\mathbf{x},t) = \alpha_{\mathbf{p}}^{*}(t)\Psi_{\mathbf{p}r}^{(+)}(\mathbf{x},t) + \beta_{\mathbf{p}}^{*}(t)\Psi_{\mathbf{p}r}^{(-)}(\mathbf{x},t),$$
(18)

$$\Phi_{\mathbf{p}r}^{(-)}(\mathbf{x},t) = \alpha_{\mathbf{p}}(t)\Psi_{\mathbf{p}r}^{(-)}(\mathbf{x},t) - \beta_{\mathbf{p}}(t)\Psi_{\mathbf{p}r}^{(+)}(\mathbf{x},t).$$
(19)

These new spinors retain the same spin structure as the original basis, i.e.,

$$\Phi_{\boldsymbol{p}r}^{(\pm)}(\boldsymbol{x},t) =$$

$$\left[i\gamma^{0}\partial_{t}-\boldsymbol{p}\cdot\boldsymbol{\gamma}+eA(t)\gamma^{3}+m\right]e^{i\boldsymbol{p}\cdot\boldsymbol{x}}\phi_{\boldsymbol{p}}^{(\pm)}(t)R_{r}.$$
(20)

Here,  $\phi_{\mathbf{p}}^{(\pm)}(t)$  denotes the mode function in the quasiparticle representation, and its evolution encodes the pair production dynamics induced by the time-dependent field.

The function  $\phi_{\mathbf{p}}^{(\lambda)}(t)$  defines the mode functions in the quasiparticle representation and is chosen according to the ansatz

$$\phi_{\mathbf{p}}^{(\pm)}(t) = \frac{e^{\mp i \Theta_{\mathbf{p}}(t)}}{\sqrt{2\omega(\mathbf{p}, t) \left[\omega(\mathbf{p}, t) \mp P(p_{\parallel}, t)\right]}},$$
 (21)

where the transverse energy  $\epsilon_{\perp}(p_{\perp})$ , the longitudinal quasi-momentum  $P(p_{\parallel},t)$  and the quasienergy  $\omega(\boldsymbol{p},t)$  are defined, respectively, as

$$\epsilon_{\perp}(p_{\perp}) = \sqrt{m^2 + p_{\perp}^2}, \qquad P(p_{\parallel}, t) = p_{\parallel} - eA(t),$$
(22)

and

$$\omega(\boldsymbol{p},t) = \sqrt{\epsilon_{\perp}^2(p_{\perp}) + P^2(p_{\parallel},t)}.$$
 (23)

The dynamical phase  $\Theta_{\mathbf{p}}(t)$  is given by

$$\Theta_{\mathbf{p}}(t) = \int_{-\tau}^{\tau} dt' \ \omega(\mathbf{p}, t'). \tag{24}$$

The functions  $\phi_{\boldsymbol{p}}^{(\pm)}(t)$  are constructed in such a way that they coincide with the standard positive and negative frequency mode functions  $\psi_{\boldsymbol{p}}^{(\pm)}(t)$  in the limit of a vanishing external electric field.

By combining (12) and (18)–(20), the spinor mode functions  $\psi_{\mathbf{p}}^{(\pm)}(t)$  can be expressed in terms of the quasiparticle basis as

$$\psi_{\mathbf{p}}^{(+)}(t) = \alpha_{\mathbf{p}}(t)\phi_{\mathbf{p}}^{(+)}(t) - \beta_{\mathbf{p}}^{*}(t)\phi_{\mathbf{p}}^{(-)}(t), \tag{25}$$

$$\psi_{\mathbf{p}}^{(-)}(t) = \beta_{\mathbf{p}}(t)\phi_{\mathbf{p}}^{(+)}(t) + \alpha_{\mathbf{p}}^{*}(t)\phi_{\mathbf{p}}^{(-)}(t). \tag{26}$$

The Bogolyubov coefficients  $\alpha_{p}(t)$  and  $\beta_{p}(t)$  are then given by

$$\alpha_{\mathbf{p}}(t) = i \,\phi_{\mathbf{p}}^{(-)}(t) \,\epsilon_{\perp}(p_{\perp}) \left(\partial_{t} - i\omega(\mathbf{p}, t)\right) \psi_{\mathbf{p}}^{(+)}(t), \tag{27}$$

$$\beta_{\mathbf{p}}(t) = -i \,\phi_{\mathbf{p}}^{(+)}(t) \,\epsilon_{\perp}(p_{\perp}) \left(\partial_{t} + i \omega(\mathbf{p}, t)\right) \psi_{\mathbf{p}}^{(+)}(t). \tag{28}$$

These expressions show that, once the spinor  $\psi_{\mathbf{p}}(t)$  is obtained from the solution of the Dirac equation (10) for a given background electric field, the Bogoliubov coefficients — and hence the particle content of the field — can be determined.

One can define the occupation number of electrons in a given eigenmode (p,r) of the field by the expectation value of the time-dependent number operator in the initial vacuum state

$$f_r(\mathbf{p}, t) = \langle 0_{\rm in} | \hat{B}_{\mathbf{p}r}^{\dagger}(t) \hat{B}_{\mathbf{p}r}(t) | 0_{\rm in} \rangle. \tag{29}$$

Similarly, the occupation number of positrons is given by

$$\bar{f}_r(-\boldsymbol{p},t) = \langle 0_{\rm in} | \hat{D}_{-\boldsymbol{p}r}^{\dagger}(t) \hat{D}_{-\boldsymbol{p}r}(t) | 0_{\rm in} \rangle. \tag{30}$$

Charge conjugation symmetry ensures the equality

$$f_r(\boldsymbol{p},t) = \bar{f}_r(-\boldsymbol{p},t). \tag{31}$$

In the quasiparticle picture, the functions  $f_r(\mathbf{p}, t)$  and  $\bar{f}_r(-\mathbf{p}, t)$  represent the time-dependent oneparticle distribution functions for electrons and positrons, respectively [18, 41].

In the absence of spin-dependent interactions, the spin index r can be omitted, and the total distribution function simplifies to

$$f(\mathbf{p}, t) = 2|\beta_{\mathbf{p}}(t)|^2, \tag{32}$$

where the factor of 2 accounts for the two-fold spin degeneracy.

#### 2.2. Electric field model

In our study of pair production, we consider a spatially homogeneous, time-dependent electric field modeled by the Sauter-type pulse [16, 42]

$$E(t) = E_0 \operatorname{sech}^2\left(\frac{t}{\tau}\right),\tag{33}$$

where  $E_0$  is the peak field strength and  $\tau$  characterizes the pulse duration. This field reaches its maximum at t=0, decreases to half of its peak

value near  $t \approx \pm 0.81\tau$ , and falls below 10% of its peak at  $t \approx \pm 2\tau$ . It asymptotically vanishes as  $|t| \gg \tau$ , while the limit  $\tau \to \infty$  corresponds to a constant electric field. The corresponding vector potential A(t) is of the form

$$A(t) = -E_0 \tau \tanh\left(\frac{t}{\tau}\right). \tag{34}$$

Though current laser technology has not yet reached the Compton-scale intensities necessary for direct experimental observation of vacuum pair production, emerging high-intensity X-ray laser sources hold promise for realizing such field strengths in the near future [10].

In the presence of the external field, the mode functions  $\psi_{p}(t)$  describing the quantum states of charged particles satisfy the equation of motion

$$\left[\partial_t^2 + ieE_0 \operatorname{sech}^2\left(\frac{t}{\tau}\right) + \omega^2(\boldsymbol{p}, t)\right] \psi_{\boldsymbol{p}}(t) = 0,$$
(35)

where  $\omega(\boldsymbol{p},t)$  is the instantaneous frequency depending on the momentum  $\boldsymbol{p}=(p_{\perp},p_{\parallel})$  and the mass m.

Two linearly independent solutions can be expressed analytically in terms of Gauss hypergeometric functions [43]

$$\psi_{\mathbf{p}}^{(+)}(y) = N^{(+)}(\mathbf{p}) y^{-i\tau\omega_0/2} (1-y)^{i\tau\omega_1/2} \times {}_2F_1(a,b,c;y),$$
(36)

$$\psi_{\mathbf{p}}^{(-)}(y) = N^{(-)}(\mathbf{p}) y^{i\tau\omega_0/2} (1-y)^{-i\tau\omega_1/2}$$

$$\times {}_{2}F_{1}(1-a, 1-b, 2-c; y),$$
(37)

where the rescaled time variable is

$$y = \frac{1}{2} \left( 1 + \tanh \frac{t}{\tau} \right),\tag{38}$$

and the asymptotic frequencies are defined by

$$\omega_0^2 = m^2 + p_\perp^2 + (p_\parallel - eE_0 \tau)^2,$$

$$\omega_1^2 = m^2 + p_\perp^2 + \left(p_{\parallel} + eE_0 \tau\right)^2. \tag{39}$$

The hypergeometric function parameters depend on the field and momenta as

$$a = -ieE_0 \tau^2 - \frac{i\tau\omega_0}{2} + \frac{i\tau\omega_1}{2},$$

$$b = 1 + ieE_0 \tau^2 - \frac{i\tau\omega_0}{2} + \frac{i\tau\omega_1}{2},$$

$$c = 1 - i\tau\omega_0.$$
(40)

The key observable characterizing pair production is the one-particle distribution function  $f(\mathbf{p},t)$ , which represents the number density of created pairs with momentum  $\mathbf{p}$  at time t. This quantity can be calculated using the Bogoliubov coefficient, as seen in (32), where the Bogoliubov coefficient  $\beta_{\mathbf{p}}(t)$  is defined in terms of the mode functions and their time derivatives, as given in (28).

In terms of the rescaled time variable y and the mode function  $\psi_{\mathbf{p}}^{(+)}(y)$ , the explicit form of the Bogoliubov coefficient reads

$$|\beta_{\mathbf{p}}(t)|^{2} = \frac{\epsilon_{\perp}^{2}(p_{\perp})}{2\omega(\mathbf{p},t)\left(\omega(\mathbf{p},t) - P(p_{\parallel},t)\right)} \left| \left(\frac{2}{\tau}y(1-y)\frac{\mathrm{d}}{\mathrm{d}y} + \mathrm{i}\,\omega(\mathbf{p},y)\right)\psi_{\mathbf{p}}^{(+)}(y) \right|^{2}.$$
(41)

Substituting the hypergeometric solutions, the distribution function becomes

$$f(\boldsymbol{p},t) = \frac{\omega(\boldsymbol{p},t) + P(p_{\parallel},t)}{2\omega_0 \left(\omega_0 - P_0\right) \omega(\boldsymbol{p},t)} \left| \frac{2}{\tau} y(1-y) \frac{ab}{c} f_1 + i \left(\omega(\boldsymbol{p},t) - (1-y)\omega_0 - y\omega_1\right) f_2 \right|^2, \tag{42}$$

where

$$f_1 = {}_2F_1(1+a,1+b,1+c;y), f_2 = {}_2F_1(a,b,c;y). (43)$$

This exact analytic expression for the time-dependent momentum distribution function  $f(\mathbf{p}, t)$  encapsulates the full dynamics of pair creation induced by the Sauter pulse.

#### 3. Result

### 3.1. Momentum spectra

We numerically investigate the time-resolved dynamics of the longitudinal momentum spectra (LMS)  $f(p_{\parallel}, p_{\perp}, t)$  of produced electron-positron pairs in the presence of a time-dependent Sauter-type electric field. The transverse momentum  $p_{\perp}$  is treated as a fixed parameter.

Figure 1 presents a detailed time evolution of the longitudinal momentum spectrum  $f(p_{\parallel}, p_{\perp} = 0, t)$ under the influence of a Sauter-type electric field with parameters  $E_0 = 0.2E_c$  and  $\tau = 12 m^{-1}$ . The snapshots span from early times  $(t = -\tau/2)$ to late times  $(t = 5\tau)$ , illustrating the full dynamical history of pair creation from the vacuum. In the early-time frames, i.e., (a)  $t = -\tau/2$ , (b) t = 0, and (c)  $t = \tau/2$ , the spectrum exhibits a smooth unimodal profile with a peak shifting from positive to negative  $p_{\parallel}$ . This drift is consistent with the evolution of the vector potential A(t), through the relation  $p_{\parallel} = -eA(t)$ . The distributions remain smooth and bell-shaped, indicative of the quasiparticle stage [21], where particles are off-shell and the field is still ramping

At  $t = \tau$  (Fig. 1d), the field strength has started to decay, and the peak moves further into negative  $p_{\parallel}$ . A sharp falloff appears on the right tail, and the overall amplitude begins to decrease. The spectrum is still single-peaked but begins to exhibit subtle deviations from Gaussianity.

By  $t=2.3\tau$  (Fig. 1e), clear interference oscillations emerge on the right flank of the spectrum. These oscillations result from the coherent superposition of particle production amplitudes from different times. Their appearance marks the onset of the stage that corresponds to the particle reaching the on-shell condition of the residual

particle stage [21, 44]. This is even more pronounced in Fig. 1f, at  $t=3\tau$ , where a second peak arises near  $p_{\parallel}\approx-2$ , and the central peak around  $p_{\parallel}=0$  becomes sharp and decorated with dense fringes. The structure seen at  $t=3.3\tau$  (Fig. 1g) confirms the bimodal nature of the distribution and the presence of strong quantum interference. This peak separation suggests two distinct particle populations, namely those created early and accelerated by the field, and those created later with less acceleration. At later times,  $t=4\tau$  and  $t=5\tau$  (Fig. 1h and i, respectively), the interference fringes fade and the spectrum stabilizes into a smooth, narrow peak at  $p_{\parallel}\approx 0$ . This freeze-in reflects the final distribution of on-shell particles — at this time, particles become real ones

Overall, Fig. 1 captures the rich quantum dynamics of vacuum pair production, from virtual fluctuations to real particle formation. The transition from smooth to oscillatory and back to smooth distributions is a hallmark of the coherent time evolution in non-perturbative QED processes.

To deepen our understanding of vacuum pair production, we investigate the influence of the transverse momentum  $p_{\perp}$  on the time evolution of the longitudinal momentum spectrum  $f(p_{\parallel}, p_{\perp}, t)$  in the presence of a time-dependent electric field, while much of the existing literature has primarily addressed the asymptotic momentum distribution  $f(p_{\parallel},p_{\perp},t\rightarrow\infty)$  for various field configurations [22, 45–49]. In particular, we analyze how transverse momentum modifies the characteristic quantum interference structure, reshapes the spectral profiles, and induces delays in the dynamical onset of pair creation. Specifically, our study considers a Sauter-type electric field with strength  $E_0 = 0.2 E_c$  and temporal width  $\tau = 10 \ m^{-1}$ . We fix the transverse momentum to representative values  $p_{\perp} = 0.3, 0.6, 0.9$  and investigate the temporal evolution of the LMS.

Figure 2 displays the LMS at various time snapshots for these transverse momentum values, revealing rich time-dependent behavior. Crucially, the evolution is characterized by three distinct stages: an initial smooth phase with quasiparticles, a quantum interference regime with oscillatory

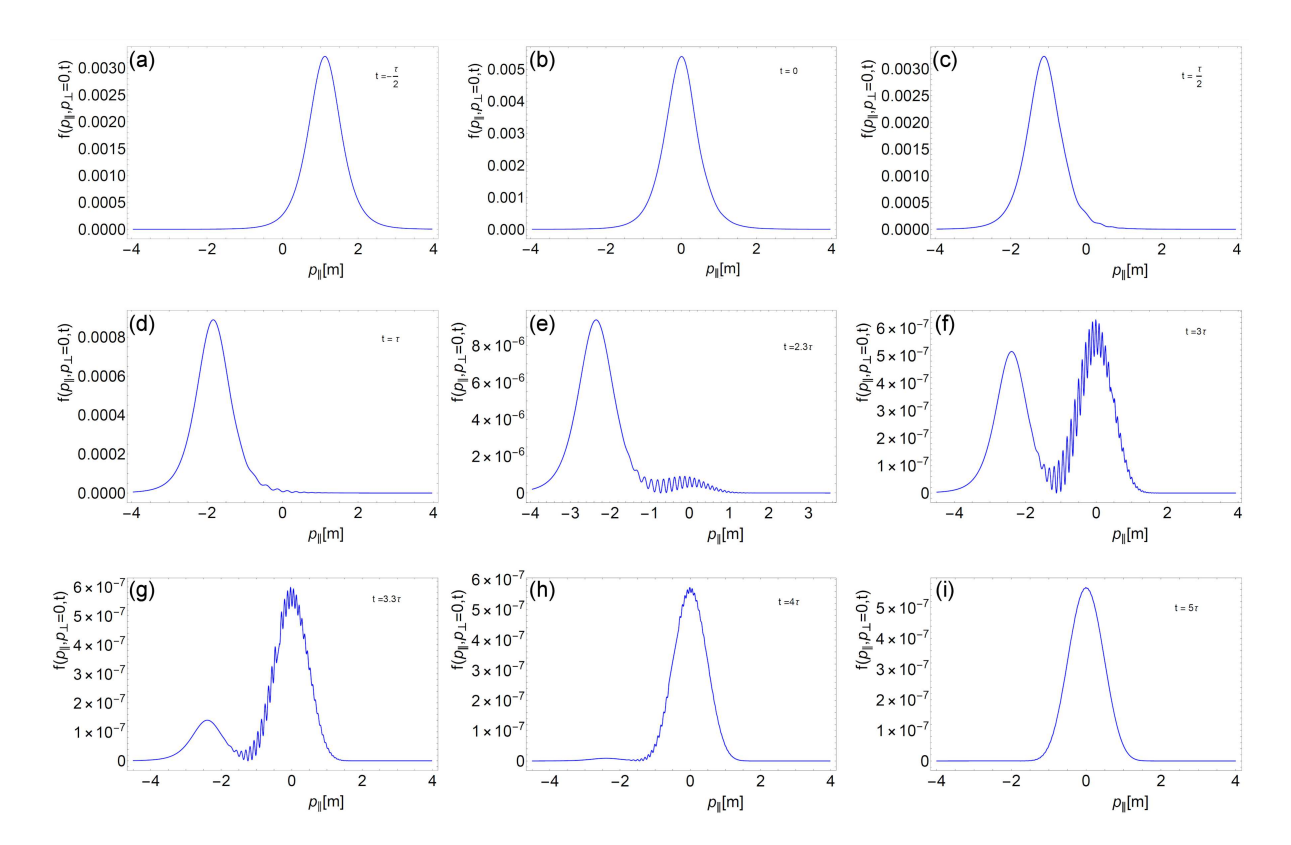


Fig. 1. (a-i) Time evolution of longitudinal momentum spectrum. The value of transverse momentum is considered to be zero, and all units are in electron mass units. The field parameters are  $E_0 = 0.2 E_c$  and  $\tau = 12 \ m^{-1}$ .

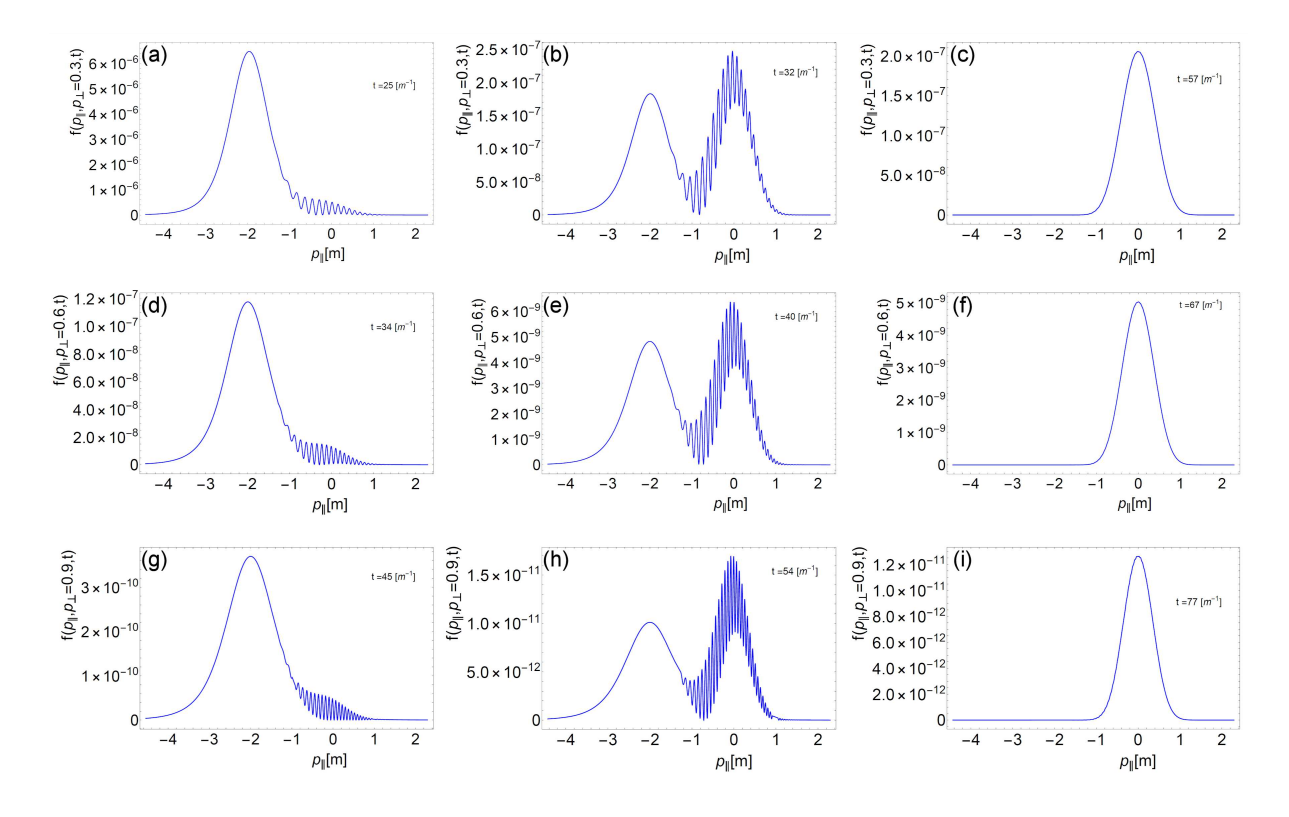


Fig. 2. Time evolution of longitudinal momentum spectrum. The transverse momentum  $p_{\perp}$  is treated as a fixed parameter, and we explore its effect on the evolution of the distribution function at representative values  $p_{\perp}=0.3,\ 0.6,\ \text{and}\ 0.9.$  All quantities are expressed in units of the electron mass. The field parameters are  $E_0=0.2\,E_c$  and  $\tau=10\ m^{-1}$ .

structures, and a final freeze-in phase dominated by on-shell pair formation. To describe these transitions, we introduce three critical time scales:

- $t_{\rm cp}$  time of central peak formation, marking the emergence of the central peak near  $p_{\parallel} \sim 0$ , indicating the onset of on-shell particle creation.
- $t_{\rm sep}$  peak separation time, where two distinct peaks become resolved in the LMS. One peak is associated with earlier creation (typically at  $p_{\parallel} < 0$ ) and the other represents new pairs centered around zero momentum.
- $t_{\rm dis}$  time at which quantum interference fringes disappear and the LMS becomes smooth and unimodal, signaling the completion of the pair creation process.

For moderate transverse momentum  $p_{\perp}=0.3$  m, the LMS at  $t=25~m^{-1}$  (Fig. 2a) is unimodal and broad, indicating the QEPP regime. The central peak forms at  $t_{\rm cp}\approx 32~m^{-1}$ , as shown in Fig. 2b, which also marks the emergence of high-frequency oscillations. The spectrum displays a pronounced bimodal structure, revealing the presence of quantum interference between different creation channels. These fringes gradually fade, and by  $t_{\rm dis}\approx 57~m^{-1}$  (Fig. 2c), the spectrum becomes sharply peaked and smooth. This indicates that coherence between different tunneling channels is lost, and the LMS reflects the final state of on-shell particles.

At higher transverse momentum  $p_{\perp}=0.6$  m, the time evolution follows the same qualitative stages, but the key time scales are significantly delayed. In Fig. 2d, at  $t=34~m^{-1}$ , early signs of a secondary central peak and oscillations are observed. These features mature in Fig. 2e at  $t_{\rm sep}\approx 40~m^{-1}$ , where a central peak dominates over the now-receding early-time peak at negative momentum. Oscillations are strong and symmetric about  $p_{\parallel}=0$ . Finally, in Fig. 2f, by  $t=67~m^{-1}$ , the LMS has fully transitioned to a single, smooth peak, identified at  $t_{\rm dis}\approx 67~m^{-1}$ .

For the largest value studied,  $p_{\perp}=0.9$  m, the effective mass is significantly higher, resulting in a substantial delay in the emergence of interference features. At  $t=45~m^{-1}$  (Fig. 2g), the spectrum is still broad and asymmetric, with faint oscillations just beginning to form. The full development of the central peak and oscillatory fringes occurs at  $t_{\rm sep}\approx 54~m^{-1}$  (Fig. 2h). This bimodal structure again shows the superposition of early and late production events. The final spectrum becomes smooth and featureless by  $t_{\rm dis}\approx 77~m^{-1}$  (Fig. 2i), completing the transition into the residual particle regime.

The key finding across all three momentum values is that the critical time scales  $t_{\rm cp}$ ,  $t_{\rm sep}$ ,  $t_{\rm dis}$  are systematically delayed as transverse momentum increases. This is because the total energy cost for pair creation grows with  $p_{\perp}$  via the

TABLE I

Effect of transverse momentum on different time scales. The time scale  $t_{\rm cp}$  corresponds to the appearance of a central peak,  $t_{\rm sep}$  is when two peaks become distinctly separated, and  $t_{\rm dis}$  indicates the disappearance of the oscillations in the LMS. All time scales are in units of  $[m^{-1}]$ .

$p_{\perp} \; [\mathrm{m}]$	$t_{\rm cp} \ [m^{-1}]$	$t_{\rm sep} \ [m^{-1}]$	$t_{ m dis}~[m^{-1}]$
0.00	22	30	50
0.30	25	32	57
0.60	34	40	67
0.90	45	54	77

relation  $\epsilon(p_{\perp}) = \sqrt{m^2 + p_{\perp}^2}$ , thereby requiring a longer duration under the electric field for the pairs to reach their on-shell condition. The central peak emerges later, the interference fringes shift to later times, and the final freeze-out is similarly delayed.

Moreover, the strength and visibility of the interference oscillations diminish slightly with increasing  $p_{\perp}$ , suggesting that transverse momentum reduces coherence between different tunneling channels. This can be physically interpreted as transverse motion suppressing the overlap between interfering wave packets in momentum space [35].

The time scales extracted from the figure analysis are summarized in Table I, illustrating their increasing trend with respect to  $p_{\perp}$ .

Table I quantitatively captures the delayed dynamical response of the system with increasing  $p_{\perp}$ , emphasizing the role of transverse degrees of freedom in modulating both the rate and coherence of pair production processes.

# 3.2. Dependence of time scales on field parameters and transverse momentum

To complement the qualitative interpretation of the longitudinal momentum spectrum, we investigate how the characteristic time scales of pair production — namely, the central peak formation  $t_{\rm cp}$ , peak separation  $t_{\rm sep}$ , and disappearance of oscillations  $t_{\rm dis}$  — depend quantitatively on external field parameters and the transverse momentum  $p_{\perp}$ . These time markers capture the dynamical phases of the pair creation process, from the emergence of on-shell pairs to the decoherence of interference structures

We numerically extracted the time scales from simulations across a range of Sauter pulse parameters, varying the field strength  $E_0$ , pulse duration  $\tau$ , and fixing transverse momentum values  $p_{\perp} \in [0, 1]$ . By fitting the results to a generalized power-law form,

$$t_i = \alpha_i \tau^{a_i} E_0^{b_i} p_{\perp}^{c_i}, \qquad (i \in \{\text{cp, sep, dis}\}), \tag{44}$$

we find excellent agreement across the parameter space. The corresponding fit coefficients  $\alpha_i, a_i, b_i, c_i$  are listed in the data table provided in the supplementary paper [50]. The resulting fit coefficients are

$$t_{\rm cp} \approx 0.4606 t_c^{-\frac{51}{25}} \tau^{\frac{8}{7}} E_0^{-\frac{5}{4}} p_{\perp}^{\frac{2}{3}},$$

$$t_{\rm sep} \approx 0.7808 t_c^{-\frac{171}{100}} \tau^{\frac{8}{9}} E_0^{-\frac{21}{20}} p_{\perp}^{\frac{7}{13}},$$

$$t_{\rm dis} \approx 2.929 t_c^{-\frac{43}{33}} \tau^{\frac{6}{7}} E_0^{-\frac{5}{6}} p_{\perp}^{\frac{1}{3}}.$$
(45)

These expressions quantitatively encode how each stage of the momentum-resolved quantum dynamics scales with the physical inputs. All three timescales increase with  $\tau$  and  $p_{\perp}$  but decrease with increasing  $E_0$ , consistent with the picture that stronger fields accelerate pair creation while transverse motion adds inertia, delaying transitions. Notably, the largest sensitivity to field strength occurs in  $t_{\rm cp}$ , reflecting how quickly pairs can emerge from the vacuum in the presence of intense electric fields. By contrast,  $t_{\rm dis}$  is less sensitive to  $p_{\perp}$ , suggesting that once interference structures form, their evolution toward asymptotic states becomes less dependent on transverse dynamics.

This hierarchy implies that the onset of coherence (i.e., interference fringes) is more heavily suppressed for large  $p_{\perp}$ , but once present, the duration and decay of these structures are altered less drastically. Since transverse momentum effectively increases the energy gap, the pair production channel opens more slowly, delaying  $t_{\rm cp}$  and consequently shifting all downstream processes.

These scaling relations provide predictive tools for controlling the dynamical window in which quantum interference is prominent. In particular, short pulses and strong fields compress the relevant timescales, enabling faster buildup and freeze-out of the LMS. Conversely, larger  $p_{\perp}$  values extend the timescales, potentially separating the dynamical phases more distinctly. This could assist in experimental resolution or enhance numerical diagnostics of intermediate quantum regimes.

Our results suggest that the observed interference structures in the momentum spectrum are sensitive probes of both temporal and momentum-space dynamics. The functional forms derived here may serve as benchmarks for strong-field QED modeling, and for calibrating analytic approximations or semiclassical interpretations of quantum tunneling in intense backgrounds.

## 4. Conclusions

We have presented a detailed dynamical study of electron—positron pair creation in a Sauter-type electric field, emphasizing the role of transverse momentum,  $p_{\perp}$ . By analyzing the longitudinal momentum spectra at various time slices and transverse momenta, we demonstrate the emergence of three

dynamical stages: the initial smooth single peak distribution, an intermediate interference-rich regime, and a final freeze-out phase. Our results show that increasing  $p_{\perp}$  leads to suppression of particle creation, delays in the onset of key features in the spectra, and modifies the width and height of the final distribution. We provide analytical expressions for the relevant time scales in terms of  $p_{\perp}$ , the pulse duration  $\tau$ , and the field strength  $E_0$ . These findings are relevant for understanding real-time dynamics in strong-field QED and can serve as a benchmark for quantum kinetic approaches to particle production.

### Acknowledgments

Deepak Sah acknowledges the financial assistance provided by the Raja Ramanna Center for Advanced Technology (RRCAT) and the Homi Bhabha National Institute (HBNI) for carrying out this research work.

#### References

- [1] P.A.M. Dirac, Proc. Roy. Soc. Lond. A 117, 610 (1928).
- [2] C.D. Anderson, *Phys. Rev.* 43, 491 (1933).
- [3] H. Euler, B. Kockel, *Naturwiss.* **23**, 246 (1935).
- [4] F. Sauter, Z. Phys. **69**, 742 (1931).
- [5] W. Heisenberg, H. Euler, Z. Phys. 98, 732 (1936).
- [6] J.S. Schwinger, *Phys. Rev.* **82**, 664 (1951).
- [7] R. Ruffini, G. Vereshchagin S.S. Xue, *Phys. Rept.* **487**, 1 (2010).
- [8] D.L. Burke, R.C. Field, G. Horton-Smith et al., *Phys. Rev. Lett.* **79**, 1626 (1997).
- [9] T. Heinzl, A. Ilderton, Eur. Phys. J. D 55, 359 (2009).
- [10] A. Ringwald, *Phys. Lett. B* **510**, 107 (2001).
- [11] L.V. Keldysh, J. Exp. Theor. Phys. 20, 1307 (1965).
- [12] E. Brezin, C. Itzykson, *Phys. Rev. D* 2, 1191 (1970).
- [13] G.V. Dunne, Eur. Phys. J. D 55, 327 (2009).
- [14] A.I. Nikishov, *Nucl. Phys. B* **21**, 346 (1970).
- [15] A. Chervyakov, H. Kleinert, *Phys. Rev. D* 80, 065010 (2009).
- [16] F. Hebenstreit, R. Alkofer, H. Gies, *Phys. Rev. D* 82, 105026 (2010).

- [17] S.A. Smolyansky, G. Ropke, S.M. Schmidt, D. Blaschke, V.D. Toneev, A.V. Prozorkevich, arXiv:hep-ph/9712377, 1997.
- [18] C. Banerjee, M.P. Singh, Phys. Rev. D 105, 076021 (2022).
- [19] S.A. Smolyansky, D.V. Churochkin,
   V.V. Dmitriev, A.D. Panferov,
   B. Kämpfer, EPJ Web Conf. 138,
   06004 (2017).
- [20] A. Otto, D. Seipt, D. Blaschke, S.A. Smolyansky, B. Kämpfer, *Phys. Rev. D* **91**, 105018 (2015).
- [21] D.B. Blaschke, S.A. Smolyansky, A. Panferov L. Juchnowski, in: Proc. of the Helmholtz Int. Summer School 2016 (HQ 2016), Dubna 2016, Eds. A. Ali, D. Blaschke, A. Issadykov, M. Ivanov, DESY-PROC, Hamburg 2017.
- [22] D.B. Blaschke, A.V. Prozorkevich, G. Ropke, C.D. Roberts, S.M. Schmidt, D.S. Shkirmanov, S.A. Smolyansky, *Eur. Phys. J. D* 55, 341 (2009).
- [23] S.A. Smolyansky, A.D. Panferov, D.B. Blaschke, L. Juchnowski, B. Kämpfer, A. Otto, Russ. Phys. J. 59, 1731 (2017).
- [24] J.H. Liu, S.K. Das, V. Greco, M. Ruggieri, Phys. Rev. D 103, 034029 (2021).
- [25] N. Tanji, Ann. Phys. **324**, 1691 (2009).
- [26] N. Tanji, Ann. Phys. 325, 2018 (2010).
- [27] I.A. Aleksandrov, A.D. Panferov, S.A. Smolyansky, *Phys. Rev. A* 103, 053107 (2021).
- [28] I.A. Aleksandrov, V.V. Dmitriev, D.G. Sevostyanov S.A. Smolyansky, Eur. Phys. J. ST 229, 3469 (2020).
- [29] E.T. Akhmedov, A.V. Anokhin, D.I. Sadekov, Int. J. Mod. Phys. A 36, 2150134 (2021).
- [30] J. Rau, B. Müller, *Phys. Rept.* **272**, 1 (1996).
- [31] J. Rau, Phys. Rev. D 50, 6911-6916 (1994).
- [32] A.B. Balantekin, J.E. Seger, S.H. Fricke, Int. J. Mod. Phys. A 6, 695 (1991).
- [33] D. Sah, M.P. Singh, in: Proc. of the XXV DAE-BRNS High Energy Physics (HEP) Symp. 2022, Mohali (India), Eds. S. Jena, A. Shivaji, V. Bhardwaj, K. Lochan, H.K. Jassal, A. Joseph, P. Khuswaha, Springer Singapore, Singapore 2024 p. 1023.

- [34] C.E. Dolby S.F. Gull, *Ann. Phys.* **297**, 315 (2002).
- [35] M. Diez, R. Alkofer, C. Kohlfürst, *Phys. Lett. B* 844, 138063 (2023).
- [36] V.I. Ritus, J. Russ. Laser Res. 6, 497 (1985).
- [37] S.M. Schmidt, D. Blaschke, G. Ropke, S.A. Smolyansky, A.V. Prozorkevich V.D. Toneev, *Int. J. Mod. Phys. E* 7, 709 (1998).
- [38] Y. Kluger, E. Mottola, J.M. Eisenberg, Phys. Rev. D 58, 125015 (1998).
- [39] W. Greiner, in: Hadrons and Heavy Ions:
  Proc. of the Summer School held at the
  University of Cape Town, Ed. W.D. Heiss,
  Springer Berlin, Heidelberg 1985 p. 95.
- [40] A.A. Grib, S.G. Mamayev, V.M. Mostepanenko, Vacuum Quantum Effects in Strong Fields, Friedmann Laboratory Publishing, 1994.
- [41] A.D. Panferov, S.A. Smolyansky, A.I. Titov, B. Kaempfer, A. Otto, D.B. Blaschke, L. Juchnowski, *EPJ Web Conf.* 138, 07004 (2017).
- [42] N.B. Narozhnyi, A.I. Nikishov, Yad. Fiz. 11, 1072 (1970).
- [43] M. Abramowitz, I.A. Stegun, Handbook of Mathematical Functions: With Formulas, Graphs, and Mathematical Tables, Applied Mathematics Series, Dover Publications, 1965.
- [44] D.B. Blaschke, L. Juchnowski, A. Otto, Particles 2, 166 (2019).
- [45] H.H. Fan, C.W. Zhang, S. Tang, B.S. Xie, Phys. Rev. D 111, 076017 (2025).
- [46] H. Al-Naseri, J. Zamanian, G. Brodin, Phys. Rev. E 104, 015207 (2021).
- [47] K. Krajewska, J.Z. Kamiński, *Phys. Rev.* A 100, 012104 (2019).
- [48] A.D. Panferov, S.A. Smolyansky, A. Otto, B. Kämpfer, D.B. Blaschke, L. Juchnowski, Eur. Phys. J. D 70, 56 (2016).
- [49] A. Bechler, F. Cajiao Vélez, K. Krajewska, J.Z. Kamiński, Acta Phys. Pol. A 143, S18 (2023).
- [50] D. Sah, M.P. Singh, Acta Phys. Pol. A 148, 149.S1 (2025).